6th AIAA Theoretical Fluid Mechanics Conference, AIAA paper 2011-3108, 27 - 30 Jun 2011, Honolulu, Hawaii

Correction on pp. 4 and 10 (in red)

Embedded LES Using PANS

Lars Davidson[1]*

[1] *Department of Applied Mechanics, Chalmers University of Technology.*
SE-412 96 Gothenburg, SWEDEN

Shia-Hui Peng[1,2]*

[2] *FOI, Swedish Defence Research Agency, SE-164 90, Stockholm, SWEDEN*

An embedded LES modelling approach is explored and verified using the PANS (Partially Averaged Navier-Stokes) model as a platform. With the same base model, the turbulence-resolving LES region is embedded by setting the PANS model coefficient to $f_k < 1$ as distinguished from its neighboring RANS region, where $f_k = 1$ is specified. The embedded LES approach is verified in computations of a turbulent channel flow and a turbulent flow over a hump. Emphasis is placed on the impact of turbulent conditions at the RANS-LES interface using anisotropic velocity fluctuations generated from synthetic turbulence. The effects of model coefficient f_k in the LES region, as well as of the spanwise size of the computational domain and the grid resolution in this direction, are also investigated. It is shown that the embedded LES method based on the PANS modelling approach is computationally feasible and able to provide reasonable turbulence-resolving predictions in the embedded LES region.

I. Introduction

It is well known that LES (Large Eddy Simulation) may become prohibitively costly when applied to wall-bounded turbulent flows at high Reynolds numbers because of the requirement of near-wall grid resolution. To circumvent this requirement, much research in past 15 years has been dedicated to the development of DES (Detached Eddy Simulation) and other similar hybrid LES-RANS methods in which the near-wall region is treated with RANS (Reynolds-Averaged Navier-Stokes) and the remaining region is covered with LES. In these methods, the RANS-LES coupling usually occurs over a surface parallel to the wall.

Another modelling approach that combines LES and RANS is *embedded* LES, in which an LES mode is embedded in any desired region, coupled with surrounding RANS simulations, and the location of the RANS-LES interaction is specified, for example over a surface normal to the streamwise direction, as shown in Figs. 1 and 2(a), respectively, for the channel flow and hump flow computed in this work. Embedded LES regions with flow separation and vortex motions are typically treated using LES, while the rest of the computational domain is covered by RANS.

The work of Quéméré and Sagaut[1] is one of the earliest on embedded LES. They computed the flow over a blunt trailing edge where LES was used in the wake region. The turbulent fluctuations at the RANS-LES interface were taken from a precursor LES simulation of channel flow. Terracol[2] used zonal RANS-LES modelling to predict the flow around an airfoil, with the intent of developing a method for predicting trailing edge noise. 2D RANS was used in the entire domain, and an LES region with a small spanwise extent was used in the wake region. Two methods for generating turbulent fluctuations at the RANS-LES interface were evaluated, namely, the recycling method and synthetic fluctuations. It was concluded that synthetic fluctuations were preferable since the recycling method introduced artificial streamwise periodic fluctuations. Mathey and Cokljat[3] studied the flow around the Ahmed body using embedded LES. The flow around the entire body was computed first using RANS. An LES was then carried out. The interface between RANS and LES was located at the position at which the rear slanting surface and the roof intersect. No turbulent fluctuations were applied at the inlet of the LES domain. Since this flow is an external flow in which the

---

*Professor, Department of Applied Mechanics, Chalmers University of Technology pressure field around the body is dependent on the flow in the entire region, it is questionable whether it is possible to decouple the RANS simulation and the LES simulation. A better approach – and also more expensive – would be to make the RANS and LES computations concurrently; a larger computational time step should probably be used in the RANS region to reduce the computational effort. Mary[4] used zonal RANS-LES to predict the flow in an internal duct. Turbulent fluctuations from a database were used and re-scaled at the RANS-to-LES interface. This work also invoked an interface from LES to RANS at which the resolved turbulent fluctuations were dampened by means of a time filter. Zhang *et al.*[5] used forcing at the interface between RANS and LES. The forcing was adjusted in order to match a prescribed Reynolds shear stress profile somewhere downstream of the RANS-LES interface. The approach was applied to channel flow and the flow around an airfoil. Forcing was also used in Ma *et al.*,[6] which was created using the SGS stress tensor from a scale-similarity model by selecting only the instantaneous SGS stress that corresponds to backscatter.[12]

In the present work, an embedded LES method is verified and applied to turbulent channel flow and a flow over a hump. In the simulation, the LES region is placed immediately after the upstream RANS region. In general, the LES region may be *embedded* in between upstream and downstream RANS regions. The emphasis in the present study is however on the RANS-LES coupling over the interface when going from an upstream RANS region to a downstream LES region as illustrated in Figs. 1 and 2(a). In this type of configuration, the critical issue in the RANS-LES coupling is how to create resolved turbulence at the interface and how to dampen modelled RANS turbulence when the flow enters the LES region. The embedded LES method investigated in this work is based on the PANS (Partially Averaged-Navier-Stokes) modelling approach,[7–9] which is a modified $k-\varepsilon$ model that operates in either RANS mode or LES mode. In this work, a low-Reynolds number (LRN) PANS model[10] is used in both the RANS and the LES regions.

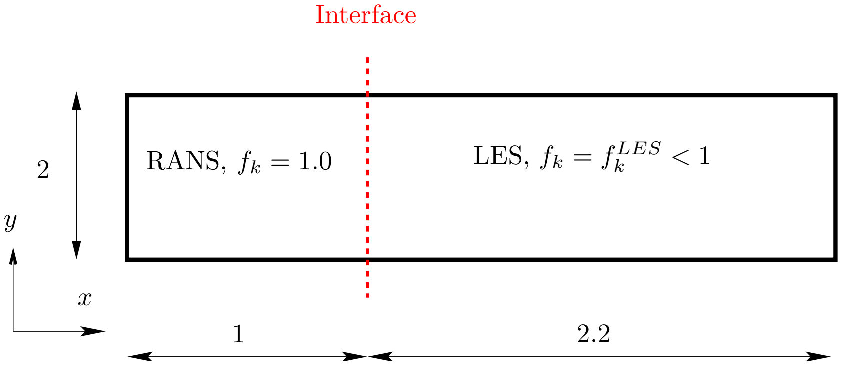

Figure 1. Channel flow configuration. The interface separates the RANS and the LES regions.

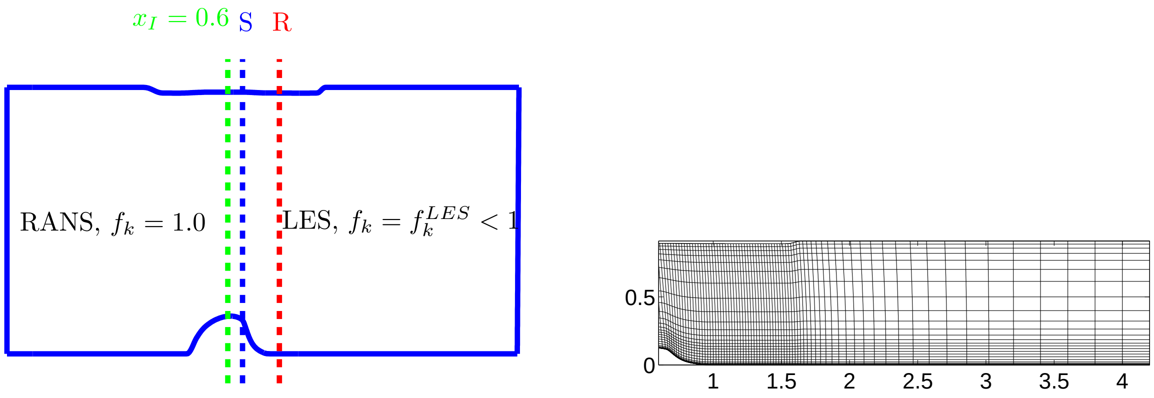

(a) Interface at $x = 0.6$, Separation $x_S = 0.65$; reattachment $x_R = 1.1$. Not to scale.

(b) LES Grid. Every 4th grid line is shown.

Figure 2. Hump flow configuration and grid schematic.

The paper is organized as follows. The PANS turbulence model is briefly introduced and the embedded modelling approach is outlined in Section II. The method for generating turbulent synthetic inlet/interface fluctuations is then presented. Next, the numerical method is presented, followed by discussion of the results in the subsequent section, and finally a summary and some concluding remarks are given.

II. PANS-Based Embedded LES

The PANS approach[7–9] uses the defined ratios of modelled and total turbulent kinetic energy and its dissipation rate, f_k and f_ε, respectively. The *partially-averaged* governing equations, invoking the PANS turbulent viscosity, ν_u, reads

$$\begin{aligned}\frac{\partial \bar{u}_i}{\partial x_i} &= 0\\ \frac{\partial \bar{u}_i}{\partial t} + \frac{\partial}{\partial x_j}\left(\bar{u}_i\bar{u}_j\right) &= -\frac{1}{\rho}\frac{\partial \bar{p}}{\partial x_i} + \frac{\partial}{\partial x_j}\left[(\nu+\nu_u)\frac{\partial \bar{u}_i}{\partial x_j}\right]\end{aligned} \tag{1}$$

A recently developed LRN PANS model is employed, for improved modelling of near-wall turbulence, which reads[10]

$$\begin{aligned}\frac{\partial k_u}{\partial t} + \frac{\partial (k_u \bar{u}_j)}{\partial x_j} &= \frac{\partial}{\partial x_j}\left[\left(\nu + \frac{\nu_u}{\sigma_{ku}}\right)\frac{\partial k_u}{\partial x_j}\right] + (P_u - \varepsilon_u)\\ \frac{\partial \varepsilon_u}{\partial t} + \frac{\partial (\varepsilon_u \bar{u}_j)}{\partial x_j} &= \frac{\partial}{\partial x_j}\left[\left(\nu + \frac{\nu_u}{\sigma_{\varepsilon u}}\right)\frac{\partial \varepsilon_u}{\partial x_j}\right] + C_{\varepsilon 1} P_u \frac{\varepsilon_u}{k_u} - C^*_{\varepsilon 2}\frac{\varepsilon_u^2}{k_u}\\ \nu_u = C_\mu f_\mu \frac{k_u^2}{\varepsilon_u}, C^*_{\varepsilon 2} &= C_{\varepsilon 1} + \boxed{\frac{f_k}{f_\varepsilon}}(C_{\varepsilon 2} f_2 - C_{\varepsilon 1}), \sigma_{ku} \equiv \sigma_k \boxed{\frac{f_k^2}{f_\varepsilon}}, \sigma_{\varepsilon u} \equiv \sigma_\varepsilon \boxed{\frac{f_k^2}{f_\varepsilon}}\end{aligned} \tag{2}$$

The modification introduced by the PANS modelling as compared to its parent RANS model is highlighted by boxes. The model constants take the same values as in the LRN model,[11] i.e.

$$C_{\varepsilon 1} = 1.5, C_{\varepsilon 2} = 1.9, \sigma_k = 1.4, \sigma_\varepsilon = 1.4, C_\mu = 0.09 \tag{3}$$

The model coefficient f_ε is set to one, and for the baseline model $f_k = 0.4$. The sensitivity to different values of f_k is investigated. The damping functions, f_2 and f_μ, have the forms, respectively, of

$$\begin{aligned}f_2 &= \left[1 - \exp\left(-\frac{y^*}{3.1}\right)\right]^2 \left\{1 - 0.3\exp\left[-\left(\frac{R_t}{6.5}\right)^2\right]\right\}\\ f_\mu &= \left[1 - \exp\left(-\frac{y^*}{14}\right)\right]^2 \left\{1 + \frac{5}{R_t^{3/4}}\exp\left[-\left(\frac{R_t}{200}\right)^2\right]\right\}\end{aligned} \tag{4}$$

At walls, $k_u = 0$ is specified. For dissipation, the value at the adjacent wall nodes with a wall distance of y is prescribed as

$$e_u = 2\nu \frac{k_u}{y^2} \tag{5}$$

For the hump flow, it was found that this boundary condition for ε_u gave numerical problems. Instead, ε_u was computed as in the one-equation hybrid LES-RANS model[12]

$$\varepsilon_u = \frac{k_u^{3/2}}{\ell}, \quad \ell = \kappa C_\mu^{-3/4} y[1 - \exp(-0.2 k_u^{1/2} y/\nu)] \tag{6}$$

with $\kappa = 0.41$.

In embedded LES, RANS is used in the first part of the domain, from the inlet to a specified x station denoted the *interface*. Figure 1 presents the flow configuration for channel flow in the first test case, where the interface is located at $x = 1$. In the RANS region, f_k in the LRN PANS model is set to one. At the interface, synthetic anisotropic fluctuations are introduced as additional source terms in the continuity and the momentum equations. In the LES region downstream of the interface, $f_k = f_k^{LES} < 1$.

All turbulence is modelled in the RANS region, since the PANS model returns to an LRN RANS model by setting $f_k = 1.0$. Consequently, the modelled values of k_u, ε_u and ν_u are large. Downstream of the interface, they must be reduced to values corresponding to LES. This is achieved by cutting off the usual convection and diffusion fluxes of k_u and ε_u through the interface. New "inlet" boundary conditions (i.e. interface conditions) are introduced additionally via sources. It is found in the channel flow computations that the interface conditions of k_u and ε_u have a large effect on the resolved turbulence downstream of the interface. Indeed, this is the case also in general when prescribing turbulent (instantaneous) inlet boundary conditions in LES or DES, where a large value of turbulent viscosity usually dampens resolved turbulence.

The turbulent conditions for k_u and ε_u at the interface are set as follows.

- The modelled turbulent kinetic, k_{inter}, is set from k_u in the RANS region, k_{RANS}, as

  $$k_{inter} = f_k^{LES} k_{RANS} \tag{7}$$

  where k_{RANS} is taken at $x = 0.5$, see Fig. 1.

- The modelled dissipation, ε_{inter}, is set from k_{inter} and an SGS length scale, ℓ_{sgs}, which is estimated from the Smagorinsky model as

  $$\ell_{sgs} = C_s \Delta \tag{8}$$

  where $\Delta = V^{1/3}$ and V is the control volume. The modelled dissipation is then approximated from

  $$\varepsilon_{inter} = C_\mu^{3/4} k_{inter}^{3/2} / \ell_{sgs} \tag{9}$$

  The influence of different values of C_s will be investigated.

k_{inter} and ε_{inter} are transported by convection and diffusion from the RANS region into the LES region through the interface.

III. Anisotropic Synthetic Turbulent Fluctuations

Anisotropic synthetic fluctuations of velocity components[13–15] are added at the interface plane. The turbulent fluctuations that are generated will be homogeneous. The method can be summarized by the following steps.

1. A Reynolds stress tensor, $\langle u_i' u_j' \rangle$, is taken from DNS data for turbulent channel flow. Since the generated turbulence is homogeneous, it is sufficient to choose one location of the DNS data. In this work, the data at $y^+ \simeq 16$ are used and, after scaling with the friction velocity, the following form is taken.

   $$\langle u_i' u_j' \rangle = \begin{bmatrix} 7.67 & -0.662 & 0 \\ -0.662 & 0.32 & 0 \\ 0 & 0 & 1.50 \end{bmatrix}$$

   This is used for both the channel and the hump test case.

2. The principal directions, η_i, are computed for the $\langle u_i' u_j' \rangle$ tensor.

3. Isotropic synthetic fluctuations, $u'_{i,iso}$, are then generated in the principal directions of $\langle u_i' u_j' \rangle$. The code for generating the isotropic fluctuations can be downloaded at
   `http://www.tfd.chalmers.se/~lada/projects/inlet-boundary-conditions/proright.html`

4. The isotropic synthetic fluctuations in the η_i directions are multiplied by the eigenvalues of $\langle u_i' u_j' \rangle$ giving a new field of fluctuations, v_i', so that $\langle v_1' v_1' \rangle \neq \langle v_2' v_2' \rangle$. Note that v_1' and v_2' are still uncorrelated, i.e. $\langle v_1' v_2' \rangle = 0$.

5. The v_i' fluctuations are transformed to the computational coordinate system, x_i; these anisotropic fluctuations are denoted $u'_{i,aniso}$. The Reynolds stress tensor of the synthetic anisotropic fluctuations is now identical to the DNS Reynolds stress tensor, i.e. $\langle u'_{i,aniso} u'_{j,aniso} \rangle = \langle u_i' u_j' \rangle$

6. Since the $u'_{i,aniso}$ are homogeneous, the Reynolds stresses, $\langle u'_{i,aniso} u'_{j,aniso} \rangle$, have constant values in the inlet plane. However, the fluctuations are dampened near the wall so as to reach a value of zero at the wall. For the hump flow, the fluctuations are also dampened in the bulk flow, see Section V.B.

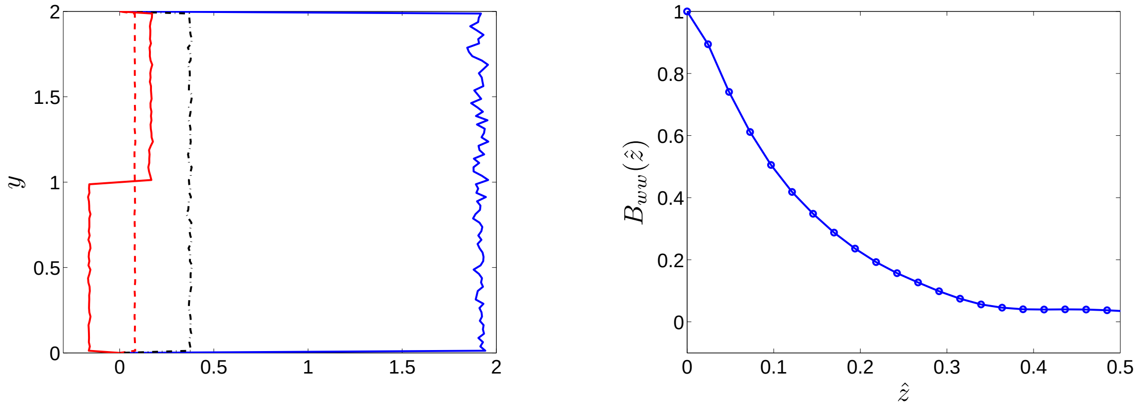

(a) —— : u^2_{rms}/u^2_τ; - - - : v^2_{rms}/u^2_τ; - · - : w^2_{rms}/u^2_τ; —— : $\langle u'v'\rangle/u^2_\tau$.

(b) Two-point correlation.

Figure 3. Channel flow – prescribed synthetic Reynolds stresses at the RANS-LES interface.

7. In the channel flow, the Reynolds shear stress changes sign across the centerline. Hence, the sign of $u'_{2,aniso}$ is changed in the upper half ($y > 1$) of the channel.

8. The correlation in time is achieved by an asymmetric time filter[16] (shown only for the streamwise fluctuation here)
$$(\mathcal{U}')^m = a(\mathcal{U}')^{m-1} + b(u'_{aniso})^m \tag{10}$$
where m is the current time step and $a = 0.954, b = (1 - a^2)^{1/2}$. Constant a is related to the integral time scale, $\mathcal{T}$, as
$$a = \exp(-\Delta t/\mathcal{T}) \tag{11}$$
where Δt is the computational time step. Constant b is given by the requirement that $\langle \mathcal{U}'^2 \rangle = \langle u'^2_{aniso} \rangle$.

Figures 3 and 4 present the Reynolds stresses of the synthetic fluctuations for the channel flow (interface fluctuations at $x = 1$) and the hump flow (inlet fluctuations at $x = 0.6$), respectively. As can be seen, they are constant (homogeneous) across the boundary layer except close to the walls, where they are dampened linearly to zero. For the hump flow, they are also dampened in the freestream region, see Section V.B. Note that the shear stress changes sign at the center of the channel as it should. The fluctuations could be scaled with, for example, a k profile from experiments or DNS. The main argument for not doing this is that the prescribed integral length scale (computed from the two-point correlation) in the y direction would then be modified. Furthermore, it was found in a previous work[16] that a re-scaling actually gives poorer predictions.

IV. Numerical Method

An incompressible, finite volume code is used in all the computations.[17] The numerical procedure is based on an implicit, fractional step technique with a multigrid pressure Poisson solver[18] and a non-staggered grid arrangement. For the momentum equations in the LES region (downstream of the interface), central differencing is used in space and the Crank-Nicolson scheme is used in the time domain. The Crank-Nicolson scheme for the pressure gradient term is found to be unstable for the hump flow and hence a fully implicit scheme is used for this term.

To prevent the imposed synthetic turbulent fluctuations at the interface from propagating upstream, a dissipative discretization scheme is used in the RANS region upstream of the interface. We use here a bounded second-order upwind van Leer scheme[19] in space, and the Crank-Nicolson scheme (except for the pressure gradient) in the time domain.

A hybrid central/upwind scheme in space and the Crank-Nicolson scheme for time discretization are used when solving for the k_u and ε_u equations in the entire domain.

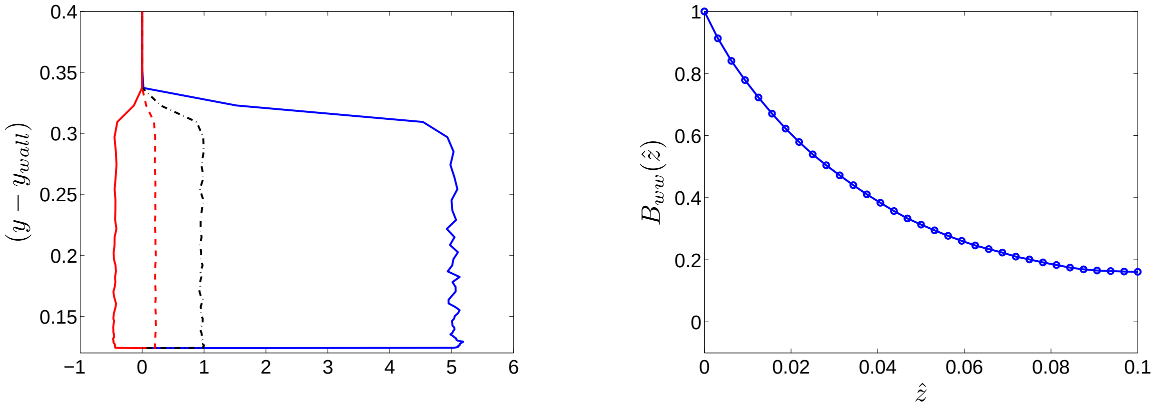

(a) —— : u^2_{rms}/u^2_τ; - - - : v^2_{rms}/u^2_τ; - · - : w^2_{rms}/u^2_τ; —— : $\langle u'v'\rangle/u^2_\tau$.

(b) Two-point correlation.

Figure 4. Hump flow – prescribed synthetic Reynolds stresses at the inlet.

V. Results and Discussion

V.A. Channel Flow

The Reynolds number for the channel flow is $Re_\tau = 950$ based on the friction velocity, u_τ, and half the channel width, δ. In the present simulations, we have set $\rho = 1$, $\delta = 1$ and $u_\tau \simeq 1$, see Fig. 1. The relatively low Reynolds number ($Re_\tau = 950$) is chosen to allow an accurate simulation of the flow when the PANS model is used in LES mode. With a $3.2 \times 2 \times 1.6$ domain, a mesh with $64 \times 80 \times 64$ cells is used in, respectively, the streamwise (x), the wall-normal (y) and the spanwise (z) direction, see Fig. 1. The resolution is approximately (the wall shear stress varies slightly along the wall) $48 \times (0.6 - 103) \times 24$ in viscous units. Inlet conditions at $x = 0$ are created by computing fully developed channel flow with the LRN PANS model in RANS mode (i.e. with $f_k = 1$).

Convective boundary conditions are used at the outflow and periodic conditions are employed in the spanwise direction. The anisotropic synthetic fluctuations described in Section III are added at the interface. The spanwise integral length scale calculated from the two-point correlation, see Fig. 3(b), of the w'_{aniso} fluctuations is 0.13. The resulting integral time scale of the synthetic fluctuations is 0.015 (the numerical time step is 0.000625). The interface condition for ε_u is computed with the baseline value $C_s = 0.07$, see Eq. 8, and the interface condition for k_u is computed from Eq. 7.

Figure 5 presents the mean velocity and the resolved shear stresses at three streamwise locations, $x = 0.19$, 1.25 and 3 (recall that the interface is located at $x = 1$). At $x = 3$, the predicted velocity agrees very well with the log-law. This suggests that the modelled turbulent shear stresses have been effectively adapted and are appropriate to enable a very good distribution of the mean flow. The resolved shear stress is – as expected – zero at the first location, which is located in the RANS region. At $x = 1.25$ (i.e. 0.25δ downstream the interface), the resolved shear stress resembles the prescribed shear stress at the interface, but its form is reasonably close to a fully developed profile at $x = 3$ (2δ downstream the interface). With a further extended channel length, it is believed that the resolved turbulence would be further re-established and the resolved turbulent shear stress should be well recovered correspondingly.

The RMS of resolved velocity fluctuations, u_{rms}, v_{rms} and w_{rms}, at $x = 3$, the peak values of u_{rms} and the turbulent viscosity versus streamwise position are presented in Fig. 6. The near-wall distribution of the RMS of velocity fluctuations is in reasonable agreement with DNS data (u_{rms} is somewhat too large). They are, however, over-predicted in the center region. This has been caused by the homogeneous fluctuations imposed at the interface. The resolved streamwise velocity fluctuations are zero in the RANS region, as shown in Fig. 6(b), of which the maximum RMS values increase sharply over the interface thanks to the imposed fluctuations. The turbulent viscosity is reduced at the interface from its peak RANS value of approximately 80 to a value relevant for LES with $\nu_{u,peak}/\nu \simeq 1$.

Figures 7 and 8 present the sensitivity to the prescribed inlet turbulent length scale, i.e. to C_s in Eq. (8). An increased length scale (equivalent to a reduced ε_u) at the interface gives, as expected, an increased

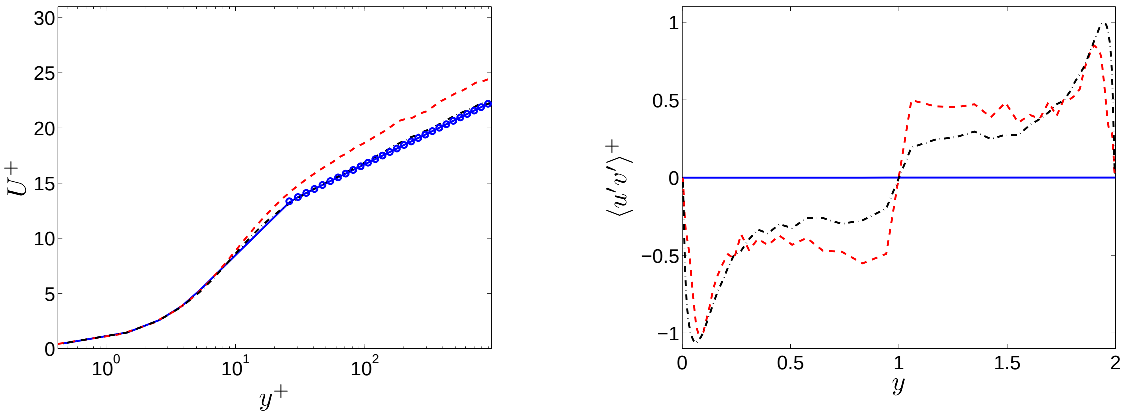

Figure 5. Channel flow. Time-averaged streamwise (U) velocity and resolved shear stresses. —— $x = 0.19$; - - - $x = 1.25$; - · - $x = 3$. The log-law is plotted in symbols.

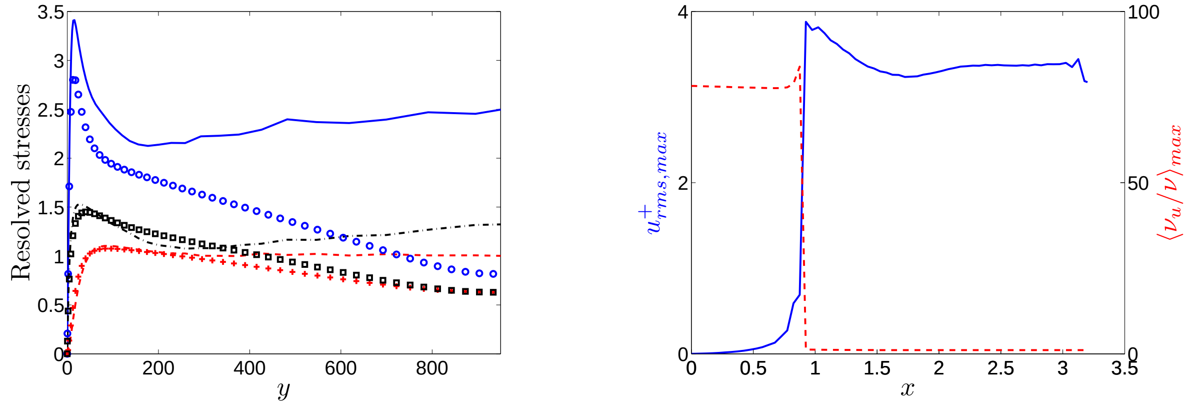

(a) $x = 3$. —— u^+_{rms}; - - - v^+_{rms}; - · - w^+_{rms}; markers: DNS data.[20]

(b) - - - : Turbulent viscosity (right y axis); —— : maximum $\langle u'u' \rangle^+$ (left y axis)

Figure 6. Channel flow. (a) Resolved normal resolved RMS fluctuations at $x = 3$; (b) Maximum u^+_{rms} and $\langle \nu_u/\nu \rangle$ versus x.

turbulent viscosity and a reduced peak of the resolved turbulent shear stress in the LES region. The baseline value, $C_s = 0.07$, gives the best results. The friction velocity, shown in Fig. 8(b) for every second node in the streamwsie direction, quickly approaches the fully developed value of $u_\tau = 1$ with $C_s = 0.07$, whereas larger values of C_s delay the re-establishment of u_τ towards $u_\tau = 1$, which instead approaches a smaller value. The reason is that the turbulent viscosity becomes so large that it tends to dampen the resolved fluctuations. If the channel were long enough, the resolved turbulence would probably be fully dampened because of too large turbulent viscosities. It is noted that, for $f_k = 0.4$, u_τ exhibits oscillations in the LES region due to the use of central differencing scheme. The same behavior was observed in previous simulations.[16] Nonetheless, this behavior never appears in simulations of a fully developed channel flow in which the oscillations are automatically suppressed by the periodic streamwise boundary conditions. For $C_s = 0.1$ and $C_s = 0.2$, note that the u_τ-distributions are shown for every second node, and hence no oscillations are presented in Fig. 8(b).

Figures 9 and 10 present predictions at $x = 3$ using different f_k values in the LES region. It is shown that both $f_k = 0.2$ and $f_k = 0.4$ give very good results and that $f_k \geq 0.6$ generates somewhat too a large modelled eddy viscosity, resulting in an over-prediction of U^+. Although not shown here, it is noted that $f_k = 0.3$ and 0.5 produce almost as good results as the baseline value of $f_k = 0.4$.

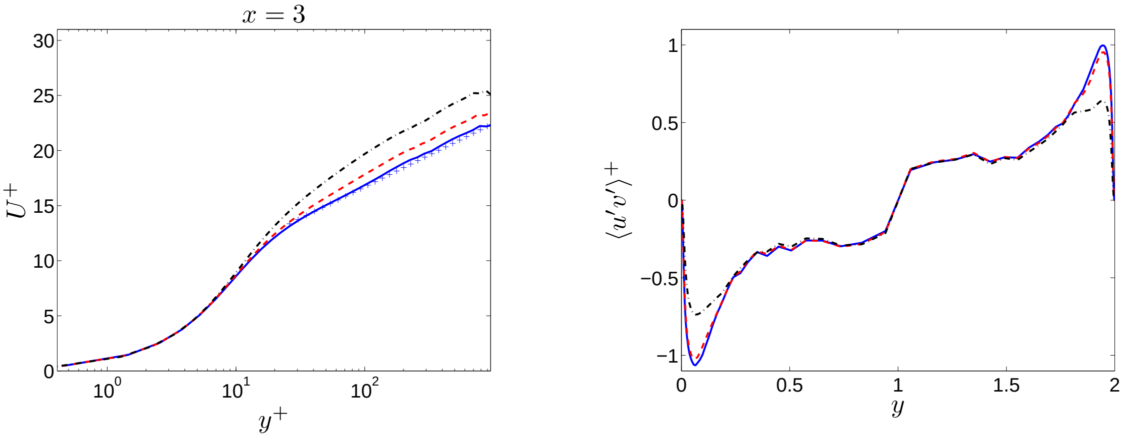

(a) Mean velocity

(b) Resolved shear stress

Figure 7. Channel flow. Sensitivity to C_S when prescribing interface ε_u condition using Eq. (8). (a) Mean velocity at $x = 3$; (b) Resolved shear stresses at $x = 3$. —— : $C_s = 0.07$; - - - : $C_s = 0.1$; -·-·- : $C_s = 0.2$.

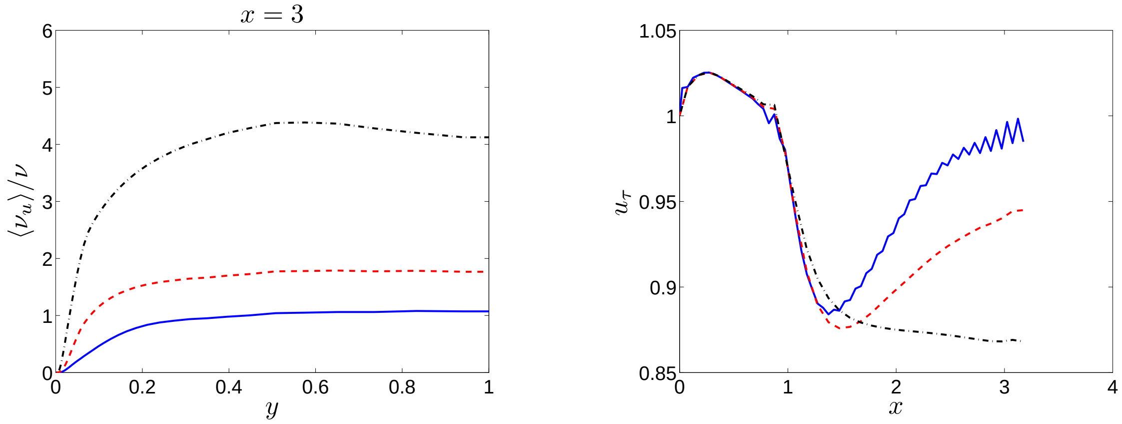

(a) Turbulent viscosity

(b) Friction velocity

Figure 8. Channel flow. Sensitivity to C_S when prescribing interface ε_u condition using Eq. (8). (a) Turbulent viscosity at $x = 3$; (b) Development of friction velocity in the streamwise direction. —— : $C_s = 0.07$; - - - : $C_s = 0.1$; -·-·- : $C_s = 0.2$.

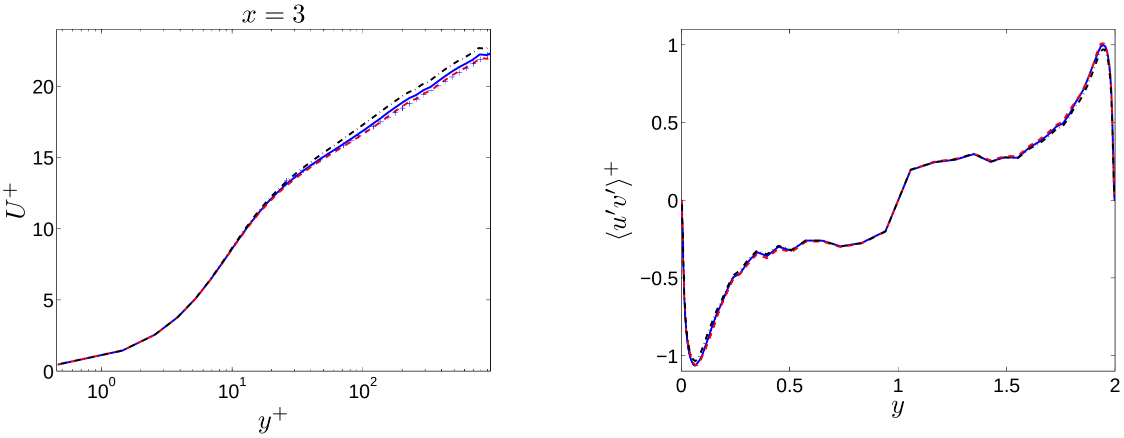

(a) Mean velocity

(b) Resolved shear stress

Figure 9. Channel flow. Sensitivity to f_k in the LES region. Mean velocity and resolved shear stresses at $x = 3$. —— : $f_k = 0.4$; - - - : $f_k = 0.2$; -·-·- : $f_k = 0.6$.

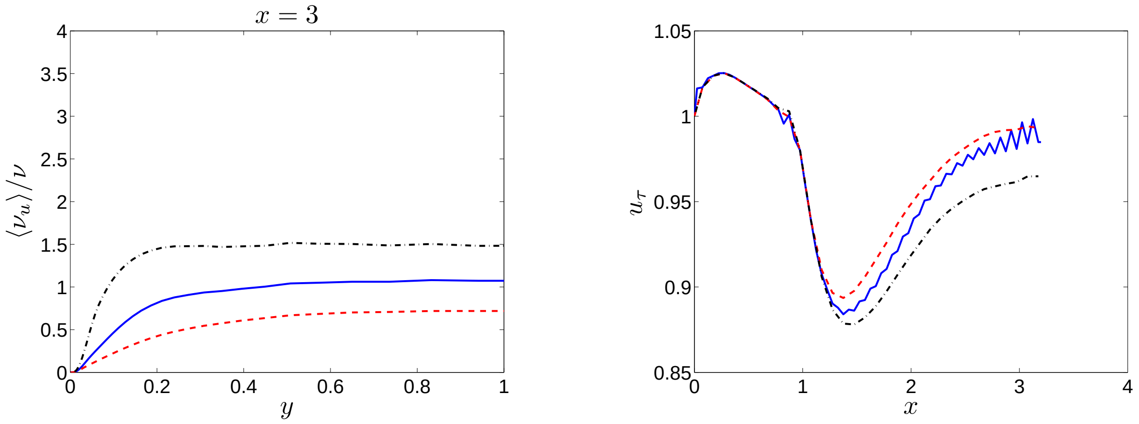

(a) Turbulent viscosity

(b) Friction velocity

Figure 10. Channel flow. Sensitivity to f_k in the LES region. (a) Turbulent viscosity at $x = 3$; (b) Development of friction velocity in the streamwise direction. —— : $f_k = 0.4$; - - - : $f_k = 0.2$; -·- : $f_k = 0.6$.

V.B. Hump flow

The hump flow has been studied previously using LES[21,22] and DES.[22] Wall functions were used in Ref. 21, whereas the near-wall flow was resolved in Ref. 22 with a refined mesh in the wall-normal directions.

The Reynolds number of the hump flow is $Re_c = 936\,000$, based on the hump length, c, and the inlet mean velocity at the centerline, $U_{in,c}$. In the present simulations, the value of ρ, c and $U_{in,c}$ have been set to unity by adapting the molecular viscosity to have the Reynolds number specified. The configuration is given in Fig. 2(a). Experiments were conducted by Greenblatt.[23,24] The maximum height of the hump, h, and the channel height, H, are given by $H/c = 0.91$ and $h/c = 0.128$, respectively. The baseline mesh has $312 \times 120 \times 64$ cells with $Z_{max} = 0.2$. The grid was created by the group of Prof. Strelets in St. Petersburg and is the mandatory grid in the ATAAC project (see Acknowledgements). The $x - y$ grid is shown in Fig. 2(b).

There are side-wall effects (3D flow) near the side plates in the experiment. Hence, in order to compensate for the blockage effect of the side plates in the computation, the surface shape of the upper wall (above the hump) is modified and the upper wall is moved slightly downwards, see Fig. 2(a). The ratio of the local cross-sectional area of the side plates (facing the flow) to the cross sectional area of the tunnel enclosed by the side plates was computed. This ratio was used to scale the local height of the channel and thus modifying the contour shape of the upper wall.

Neumann conditions are used at the outflow section located at $x = 4.2$. Slip conditions are used at the upper wall and symmetric boundary conditions are used on the spanwise boundaries. Inflow boundary (at $x = 0$) conditions are taken from 2D RANS SST $k - \omega$ simulations carried out by the group of Prof. Strelets in St. Petersburg. The distributions of U and V at $x = 0.6$ from the the RANS simulation are used together with $W = 0$ as mean inlet velocities to which the fluctuating velocity $\mathcal{U}'$, $\mathcal{V}'$ and $\mathcal{W}'$, obtained with Eq. (10), are superimposed. The computed integral length scale for the synthetic inlet fluctuations is $\mathcal{L} \simeq 0.040$ (see the two-point correlation in Fig. 4(b)) and the integral time scale $\mathcal{T} \simeq 0.038$. It is noted that the prescribed inlet integral length scale is rather large (approximately equal to the inflow boundary layer thickness). The reason is that synthetic fluctuations with a large integral length scale are efficient in generating resolved turbulent fluctuations.[16]

The inlet fluctuations, $\mathcal{U}'$, $\mathcal{V}'$ and $\mathcal{W}'$, are reduced to zero in the off-wall region by multiplication of the blending function f_{bl}

$$f_{bl} = \max\left\{0.5\left[1 - \tanh\left(\frac{y - y_{bl} - y_{wall}}{B}\right)\right], D\right\}, \quad y_{bl} = 0.2, \quad B = 0.01 \tag{12}$$

This makes the fluctuations go to zero at the distance of $y_{bl} \simeq 0.2$ from the wall over the distance $B = 0.01$, see Fig. 4. The freestream turbulence is determined by D, which takes a values of $D = 0.02$. The inlet boundary condition for ε_u is computed with the baseline value $C_s = 0.1$, see Eq. 8, and the inlet condition for k_u is computed from Eq. 7.

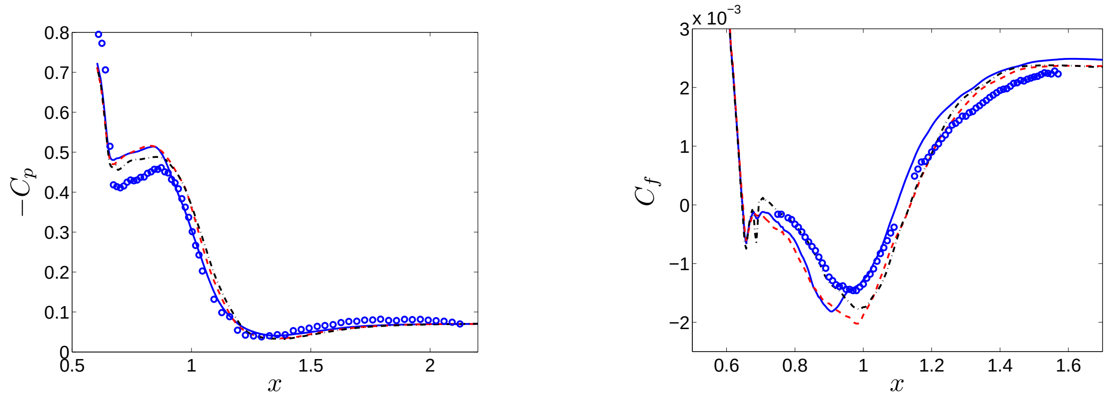

Figure 11. Hump Flow. (a) Pressure coefficient; (b) Skin friction. —— : baseline inlet fluctuations (see Fig. 4); - - - : 1.5× (baseline inlet fluctuations); -·-·- : 0.5× (baseline inlet fluctuations); ○: experiments.

The time step is set to $\Delta t = 0.002$. Before averaging is started, 7500 time steps are run and sampling is then done for 7500 time steps. The entire CPU time on one core standard Linux machine is approximately 100 hours.

Note that, by mistake, all hump flow simulations were carried out with $\sigma_{k,u} = \sigma_k$ and $\sigma_{\varepsilon,u} = \sigma_\varepsilon$, see Eq. 2.

Figures 11–14 present results obtained with different magnitudes of the synthetic turbulent inlet fluctuations. Three different magnitudes are used: the baseline value (see Fig. 4(a)), and 50% larger and 50% smaller, respectively, than the baseline value. All three predictions give fairly good agreement with experiments. It is shown that the larger the inlet fluctuations, the stronger the recirculation on the lee side of the hump. This is somewhat unexpected, since one would expect that large inlet fluctuations should generate large resolved shear stresses leading to a small recirculation region. However, as Fig. 13 shows, large inlet fluctuations do actually not produce the largest resolved shear stresses in the backflow region. The skin friction confirms that the backflow is the strongest for the large inlet fluctuations. It can also be seen in Fig. 11(b) that the peak in the backflow occurs slightly earlier for the baseline case as compared to the other cases. There seems to be a strange behavior in C_f for the case with small inlet fluctuations which give two negative peaks in C_f in the region $0.65 < x < 0.7$ compared to only one for the other two cases, see Fig. 11(b). This is discussed in more details below in connection to Fig. 16. The pressure plateau in the recirculation (Fig. 11(a)) becomes higher for the baseline case and for the case with strong inlet fluctuations. This reflects that the early backflow in the former case and the strong backflow in the recirculation bubble in the latter case must be compensated with a larger velocity in the bulk flow.

The distributions of mean streamwise velocity plotted at different stations, as shown in Fig. 12, correspond well to the distribution of C_f in Fig. 11(b). Except for the backflow in the recirculation bubble, the difference in the predicted mean flow is only marginal due to different magnitudes of inflow velocity fluctuations. The recovery of the outer part of the boundary layer after the recirculation is somewhat slow in all three predictions, as compared to the experimental measurement.

As expected, shortly after the inflow section, the resolved shear stress increases for increasing magnitude of inlet fluctuations, see Fig. 13 at $x = 0.65$. It is noted that, at $x = 0.65$, large unphysical resolved shear stress arises in the bulk flow region. It is believed that this is due to the use of the central differencing scheme. The unphysical fluctuations decrease with increasing synthetic inlet fluctuations. The reason is simply that central differencing works well in flow regions with resolved turbulence but not in regions without resolved turbulence. However, in the outer region ($y > 0.3$) there are no unphysical oscillations. The reason is probably that the mean velocity gradients are negligible in this region and hence no oscillations are triggered. It should be noted that, already at $x = 0.8$, the unphysical fluctuations at $y < 0.3$ have disappeared. At $x = 1.1$ and further downstream, the turbulent flow has nearly been re-established with little historical effect of inlet fluctuations, where different magnitudes of inflow turbulent fluctuations have produced similar levels of resolved shear stress that are larger overall than the measured data in the outer part of the recovering boundary layer.

The turbulent viscosities depend only weakly on the magnitude of the inlet fluctuations, as shown in Fig. 14. Large inlet fluctuations do generate slightly large turbulent viscosities when the flow is re-adapting

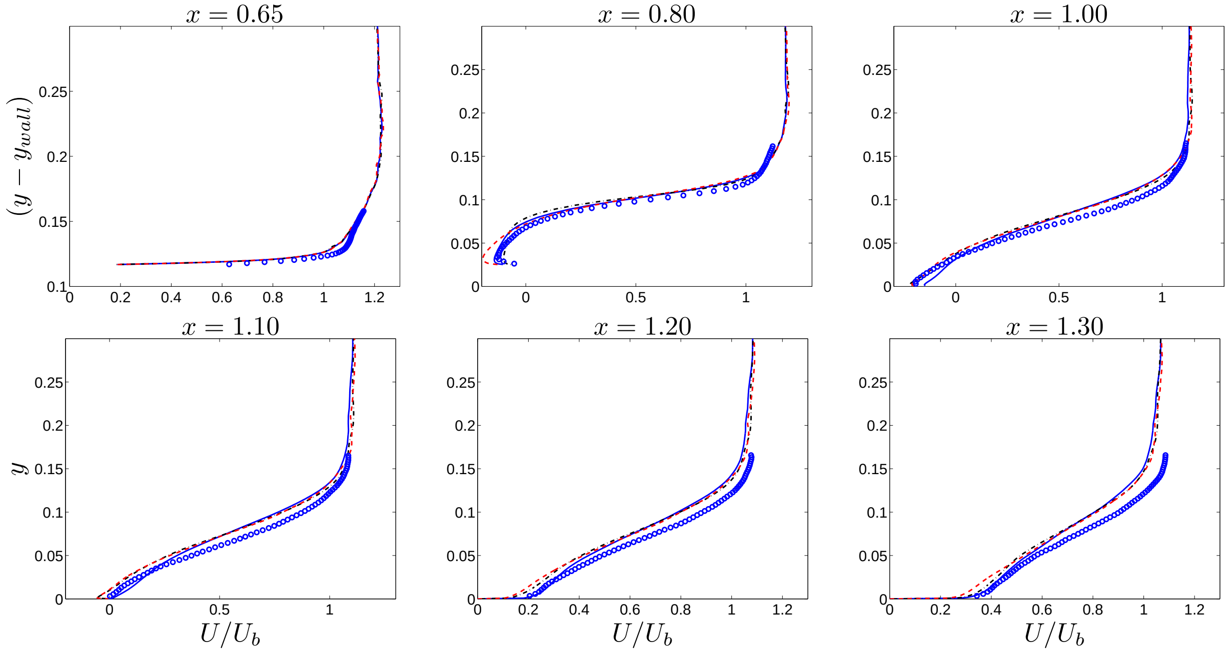

Figure 12. Hump flow: Mean velocity, $\langle \bar{u} \rangle$ ——— : baseline inlet fluctuations (see Fig. 4); - - - : 1.5× (baseline inlet fluctuations); - · - : 0.5× (baseline inlet fluctuations); ○: experiments.

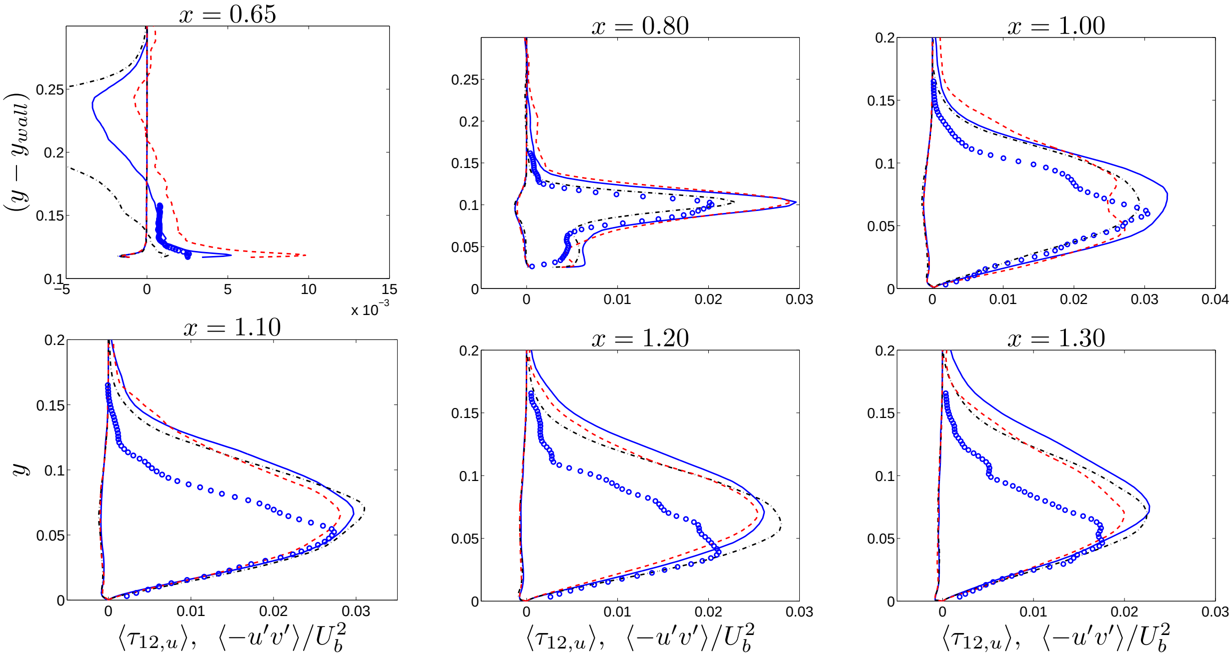

Figure 13. Hump flow: resolved and modelled shear stresses. ——— : baseline inlet fluctuations (see Fig. 4); - - - : 1.5× (baseline inlet fluctuations); - · - : 0.5× (baseline inlet fluctuations); ○: experiments.

over a short distance after the inflow section. Although the ratio of the turbulent viscosities to the molecular viscosity exceeds 100, Fig. 13 shows that the modelled shear stress is several orders of magnitude smaller than the resolved one.

Figures 15 – 19 further present a comparison of another set of three predictions. These include a computation using a refined mesh in the spanwise direction ($N_k = 128$) and imposing baseline inlet fluctuations, a computation conducted without inlet fluctuations and a computation using $f_k = 0.5$ with baseline inlet fluctuations. Simulations with $f_k = 0.3$ were also carried out, but they diverged when baseline inlet fluctuations were imposed.

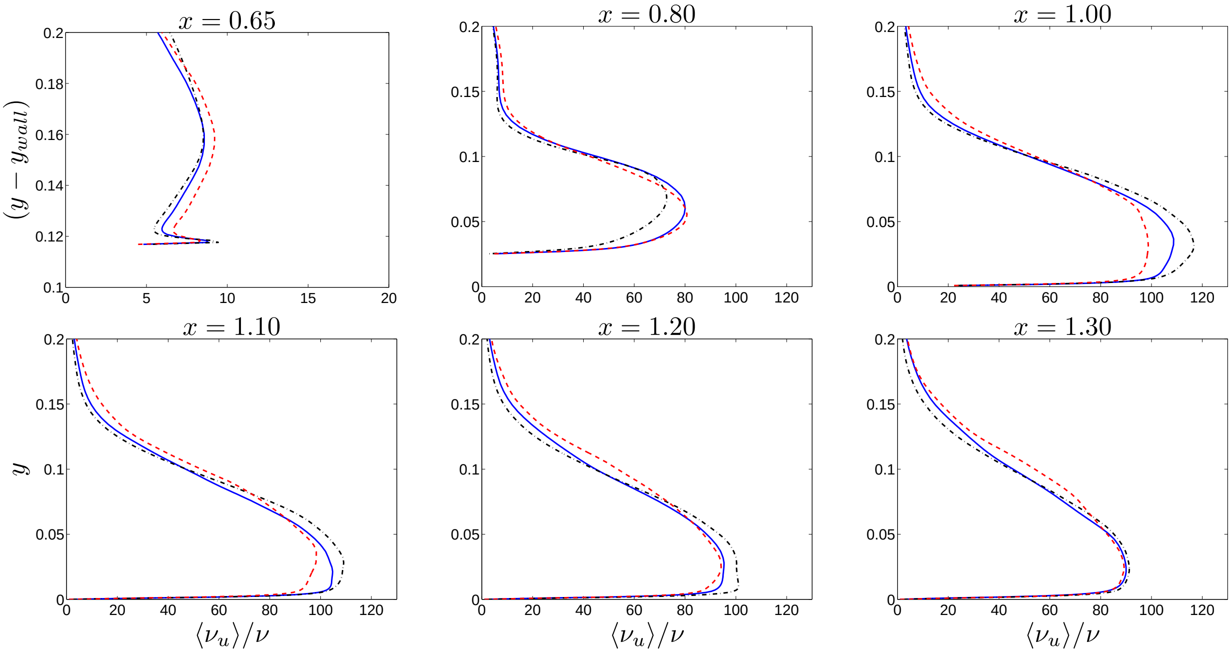

Figure 14. Hump flow: modelled turbulent eddy viscosity. —— : baseline inlet fluctuations (see Fig. 4); - - - : 1.5× (baseline inlet fluctuations); - · - : 0.5× (baseline inlet fluctuations).

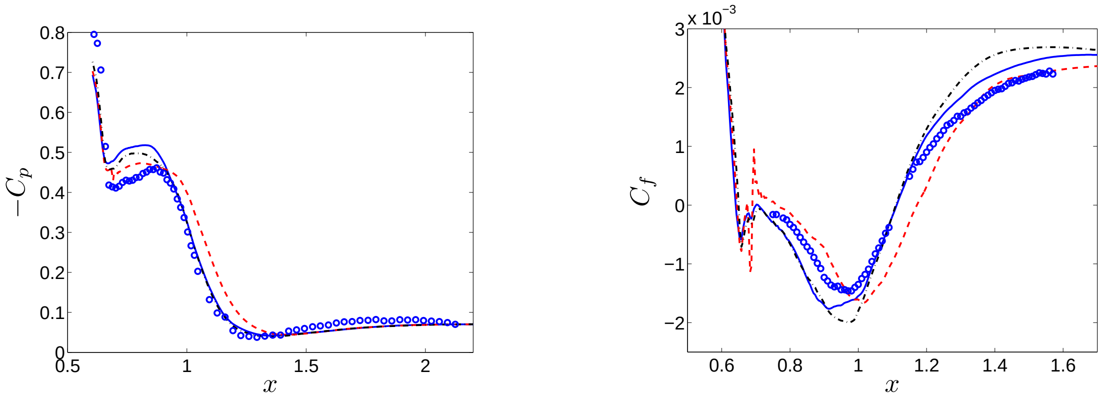

Figure 15. Hump flow. (a) Pressure coefficient; (b) Skin friction. —— : $N_k = 128$; - - - : no inlet fluctuations; - · - : $f_k = 0.5$. ○: experiments.

Without imposing turbulent fluctuations at the inlet, the resolved near-wall shear stress at $x = 0.65$ (see Fig. 18) near the inlet is small. As a consequence, the resolved turbulence in the shear layer is also very small, and hence the recirculation bubble is poorly predicted, as shown in Fig. 15(b) for the C_f distribution and the velocity profile at $x = 0.8$ in Fig. 17. The separation bubble on the lee side of the hump shifts downstream, as is clearly illustrated in the distributions of C_p and C_f in Fig. 15. Downstream of the recirculation region, the boundary layer recovery is poorly predicted and is slower than for the baseline case shown in Fig. 12.

A double peak in C_f at $x \simeq 0.67$ is seen in Fig. 15(b). This was also found in the case when small inlet fluctuations were used, see Fig. 11(b), although the peaks in the latter case are smaller. Figure 16 presents the mean velocity vector field in the region $0.65 < x < 0.75$. For the baseline case (Fig. 16(a)), the separation takes place at $x \simeq 0.65$ and downstream of this point there is a nice smooth backflow region. However, for the case with no inlet fluctuation (Fig. 16(b)), a small recirculation bubble centered at $x \simeq 0.67$ is formed and downstream of that another counter-rotating recirculation bubble, poorly resolved, is embedded beneath the large recirculation bubble. It is believed that these flow properties are unphysic and have been caused by the resolved shear stresses that are too small. With insufficient, or even with no, inflow fluctuations imposed,

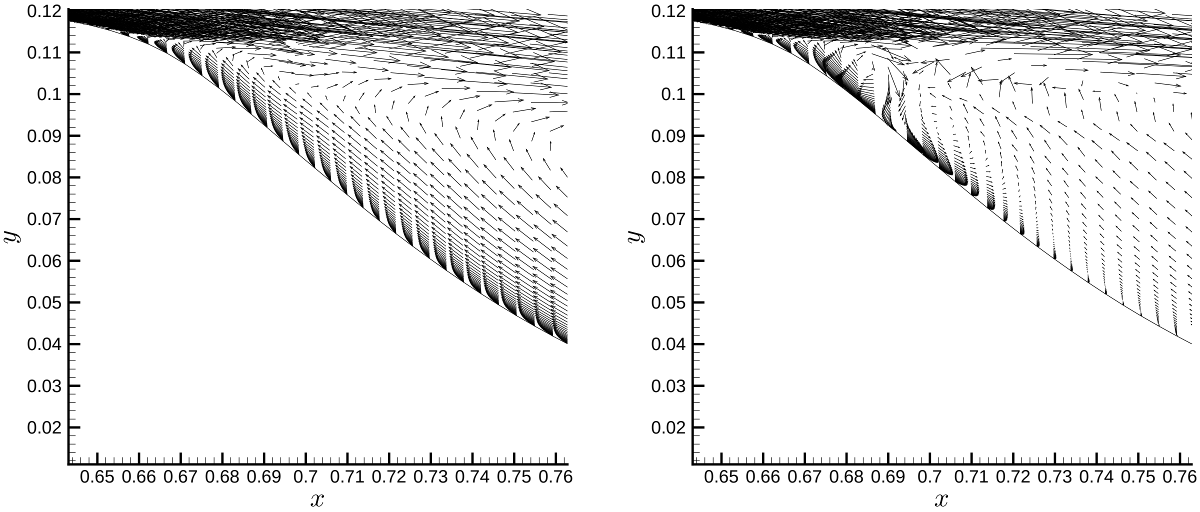

(a) Baseline case.

(b) No inlet fluctuations.

Figure 16. Vector plot.

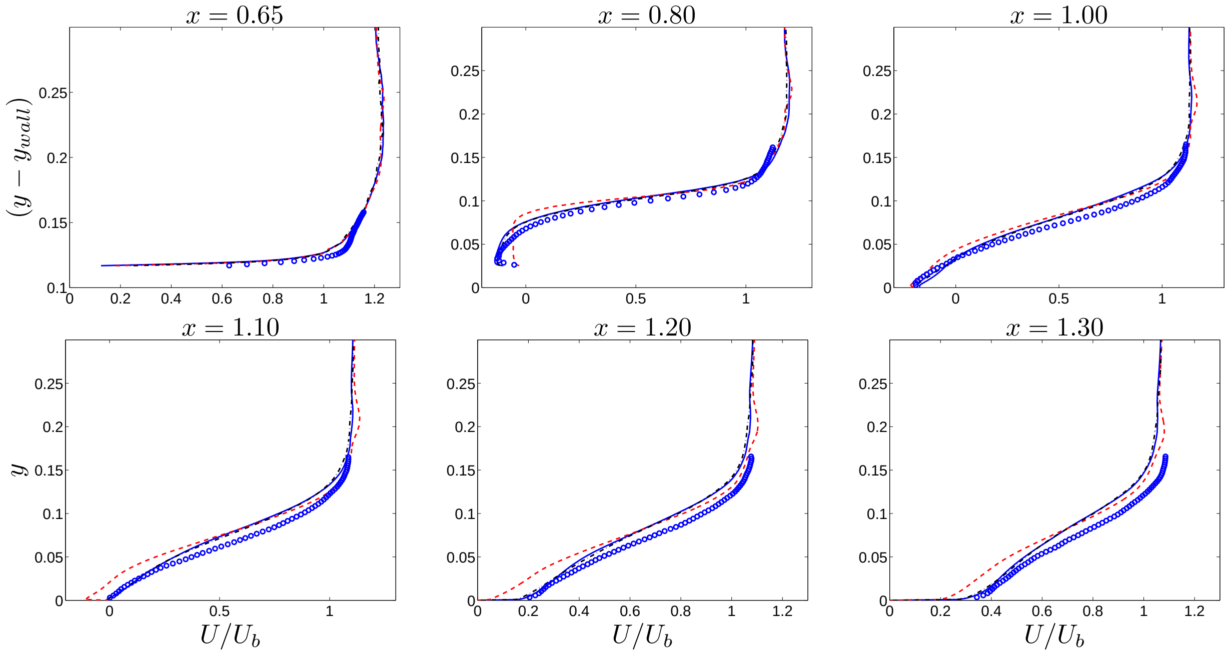

Figure 17. Hump flow. Mean velocity, $\langle \bar{u} \rangle$ —— : $N_k = 128$; - - - : no inlet fluctuations; - - - : $f_k = 0.5$. ○: experiments.

the free shear layer above the separation bubble has become less diffusive and, consequently, inducing a somewhat delayed reattachment, as shown in Fig. 15(b) and Fig. 11(b). The reverse flow in the recirculation bubble starts thus at a further downstream location as compared to that computed with relatively large inlet flow fluctuations, leading to an earlier loss of momentum in the near-wall backflow. This has facilitated the presence of the two small bubbles over the upper part of the lee side of the hump. The reason for the small resolved shear stresses is that no resolved turbulence is injected at the inlet for this case. The mean velocity vector field shown in Fig. 16(b) is similar to that for the case with small inlet fluctuations (see C_f curve in Fig. 11(b)), but in the latter case there is no second counter-rotating bubble.

The predicted velocity profiles using a fine grid in the spanwise direction ($N_k = 128$) are very similar to the ones obtained with the baseline case ($N_k = 64$). This suggests that the spanwise resolution in the baseline case is sufficiently fine. With $N_k = 128$, the backflow in the predicted recirculation region is – as in the baseline case – relatively strong on the lee side of the hump. The main difference between the two cases

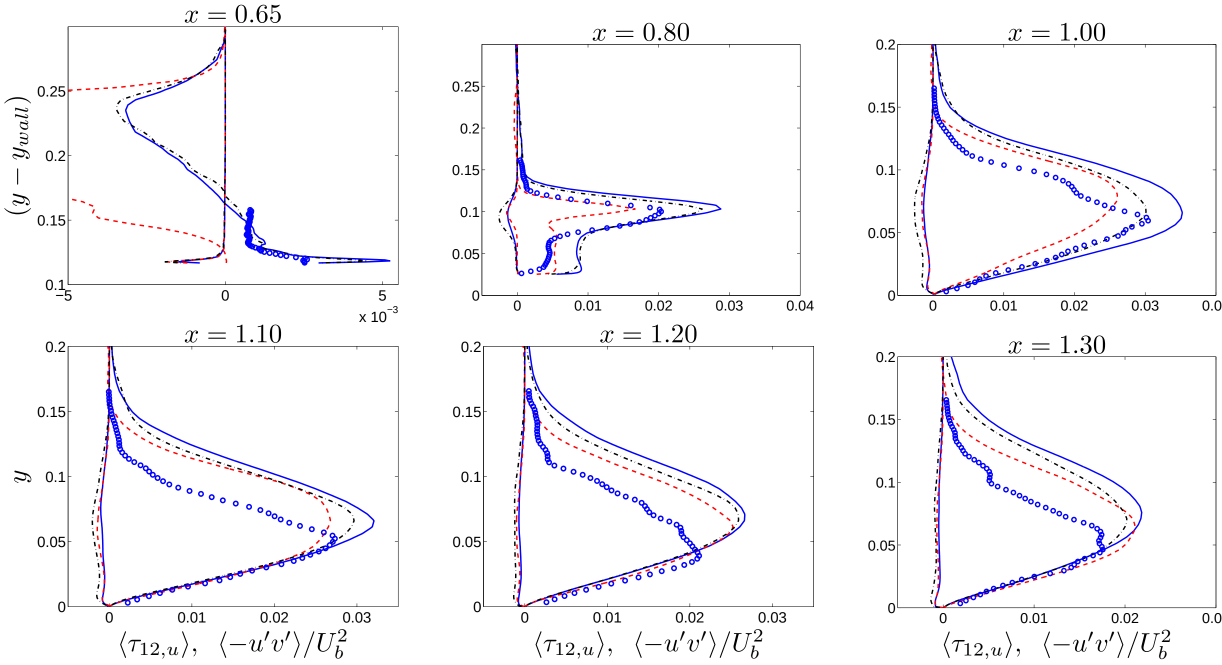

Figure 18. Hump flow. Resolved and modelled shear stresses. —— : $N_k = 128$; - - - : no inlet fluctuations; -·-· : $f_k = 0.5$. ○: experiments.

is that the fine mesh gives larger resolved shear stresses, especially near the inlet.

Increasing f_k to 0.5 has only a small impact on the predicted results. The velocity profiles are almost identical. The skin friction shows, that with $f_k = 0.5$ the location of the C_f-peak in the backflow region agrees somewhat better than with $f_k = 0.4$. Referring to Fig. 13, Fig. 18 shows further that the resolved turbulent stresses using $f_k = 0.5$ are smaller. This is consistent to the inherent PANS modelling mechanism, namely, a larger f_k value reduces the resolved turbulence. As expected, the turbulent viscosity is larger with $f_k = 0.5$ than with $f_k = 0.4$, see Fig. 19, although the difference (a factor of two), is perhaps surprisingly large. As noted above, nonetheless, the modelled stress is much smaller than the resolved one, see Fig. 18, and this is why a change in the turbulent viscosity has negligible impact on the prediction of mean flow.

The spanwise extent of the computational domain for all cases presented above was $Z_{max} = 0.2$. To investigate whether this is large enough, longitudinal spanwise two-point correlations are presented in Fig. 20. Two streamwise positions at which the two-point correlation was found to be the largest are shown, namely at $x = 0.86$ and $x = 2.56$. Three wall-normal locations are chosen. As can be seen, the two-point correlations do not always fall down to zero as they should. At $x = 0.86$ and $y - y_{wall} = 0.00085$, a large negative correlation persists for a large separation distance, $\hat{z} = z$. It is slightly worse near the outlet at $x = 2.56$ Both positive and negative correlations are found at a large separation distance of about $\hat{z} = 0.1$.

To further evaluate the possible effect of the spanwise extent, an additional simulation with $N_k = 128$ is carried out by extending the spanwise size twice as large as the baseline case. The results are presented in Figs. 21 and 22. It can be seen that the results are very similar to the baseline simulations. Two additional simulations are also included in the figures, where the influence of the integral length scale of the prescribed turbulent synthetic inlet fluctuations (see Fig. 4) is reduced by a factor of four and increased by a factor of two, respectively. It was found (not shown) that a reduction of the prescribed integral length scale by a factor of two gives negligible effect. Figure 21 shows that reducing the integral length scales has a similar tendency of effects as using no inlet fluctuations at all (cf. Fig. 17). The large recirculation bubble shifts downstream with a delayed reattachment, after which the flow recovery becomes overall slow, see Fig. 22. Increasing the inlet integral scale by a factor of two leads to relatively large resolved shear stresses and, consequently, a more diffusive free shear layer, making a relatively short recirculation region (namely, earlier reattachment).

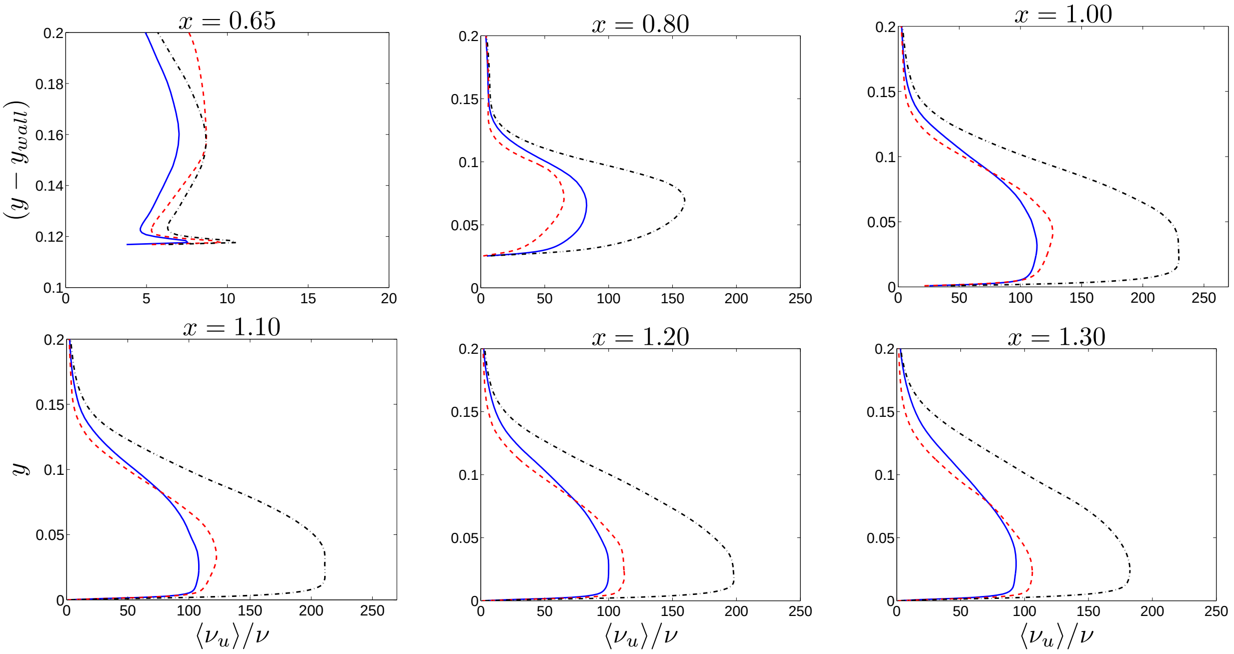

Figure 19. Hump flow. Turbulent viscosity. —— : $N_k = 128$; - - - : **no inlet fluctuations;** -·-· : $f_k = 0.5$.

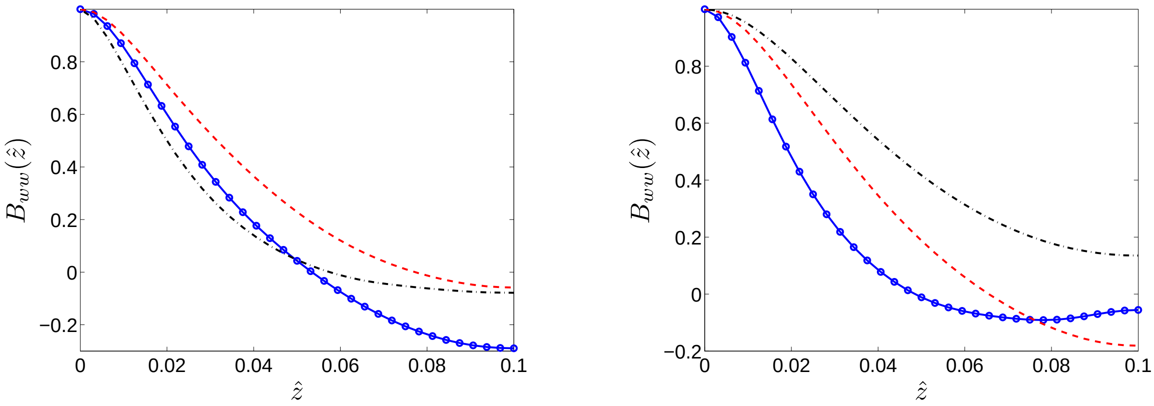

(a) $x = 0.86$.

(b) $x = 2.56$.

Figure 20. Hump flow. Two-point correlations. —— : $y - y_{wall} = 0.00085$; - - - : $y - y_{wall} = 0.014$; -·-· : $y - y_{wall} = 0.10$. **Markers indicate the grid spanwise resolution.**

VI. Summary and Concluding Remarks

By adapting the model coefficient (typically, f_k) and the grid resolution, the PANS approach may function as a RANS model or in its LES fashion. Using this inherent modelling mechanism, a PANS-based embedded LES method is presented. In the RANS region, f_k in the PANS formulation was set to one, and it was set to a smaller value in the LES region (baseline value $f_k^{LES} = 0.4$). An emphasis has been placed on the effect synthetic anisotropic fluctuations imposed at the RANS-LES interface. The method has been verified in computations of turbulent channel flow and hump flow.

For the channel flow, it was found that the addition of anisotropic fluctuations at the RANS-LES interface is very effective to *force* an efficient re-establishment towards fully developed turbulence and, consequently, enabling reasonably resolved turbulent fluctuations in the downstream LES region. Already at two half-channel widths downstream of the interface, the resolved turbulence agrees rather well with DNS data, and the wall friction velocity has reached 99% of its fully developed value. The treatment of the modelled k_u and

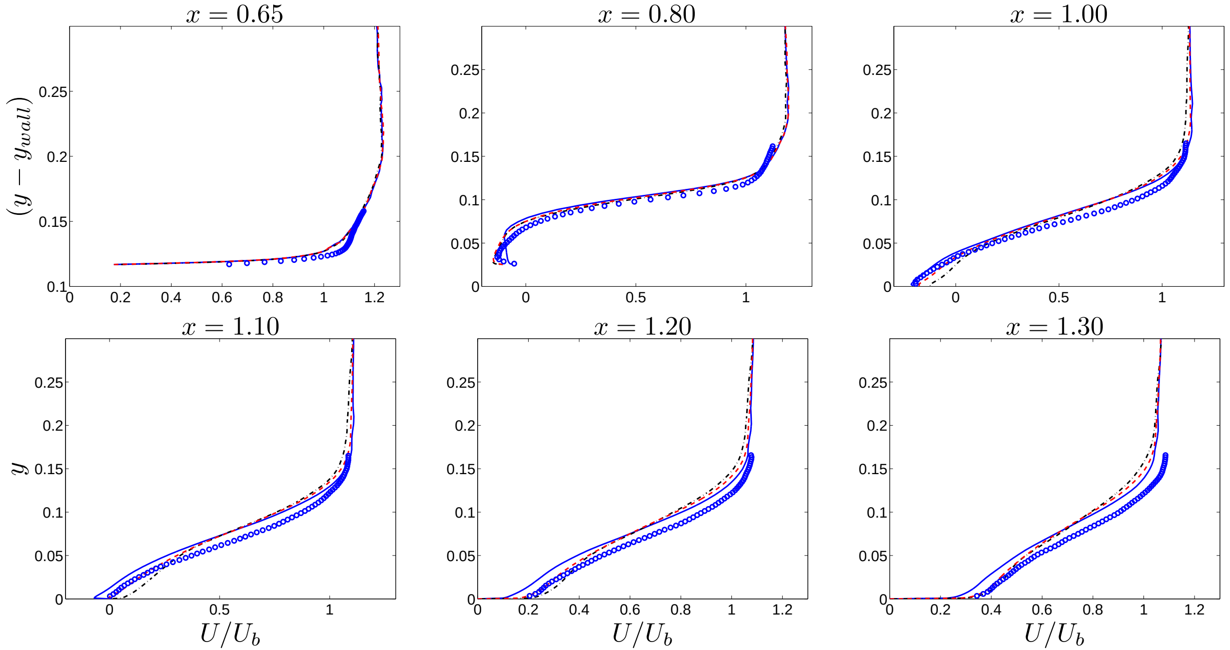

Figure 21. Hump flow. Mean velocity, $\langle\bar{u}\rangle$ —— : 0.25× (baseline inlet length scale); - - - : $N_k = 128$, $Z_{max} = 0.4$; - . - : 2× (baseline inlet length scale); ○: experiments.

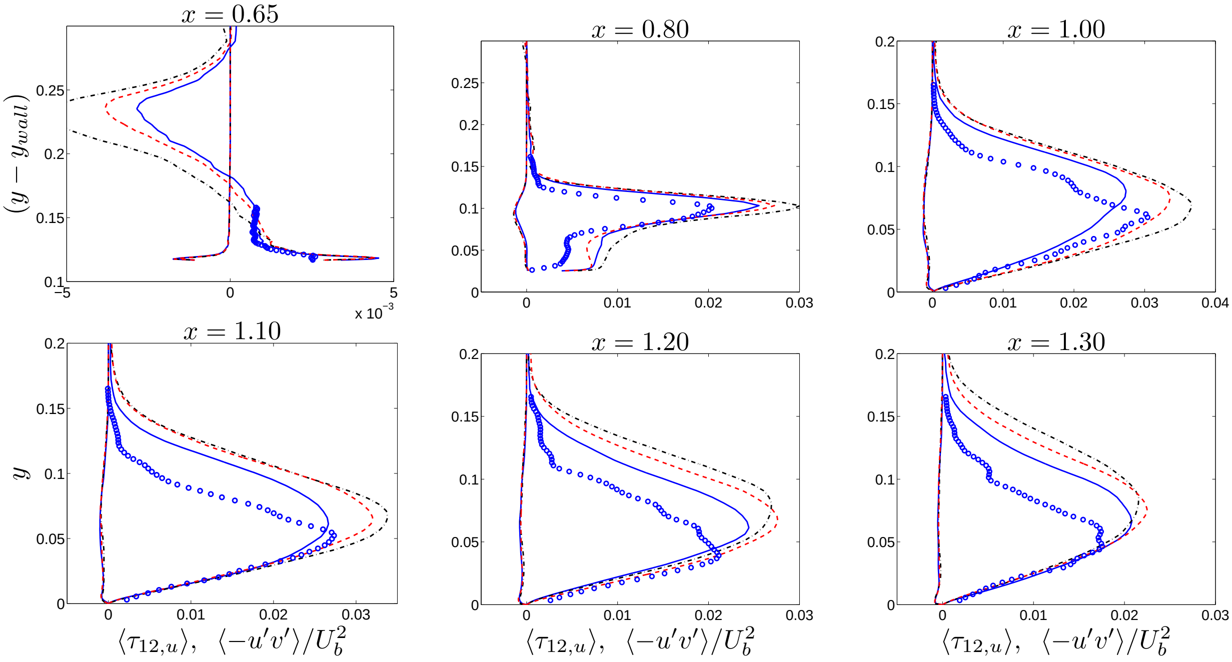

Figure 22. Hump flow. Resolved and modelled shear stresses. —— : 0.25× (baseline inlet length scale); - - - : $N_k = 128$, $Z_{max} = 0.4$ (with baseline inlet length scale); - . - : 2× (baseline inlet length scale); ○: experiments.

ε_u across the interface is important. New "inlet" (to the LES region) values of k_u and ε_u were prescribed at the interface by cutting off the usual convection and diffusion at the interface and introducing sources that correspond to convection and diffusion of interface values, k_{inter} and ε_{inter}, into the LES region. The former was set to $f_k^{LES} k_{RANS}$ and the latter to $C_\mu^{3/4} k_{inter}^{3/2}/\ell_{sgs}$ where $\ell_{sgs} = C_s \Delta$ was taken from the Smagorinsky model and a baseline value of $C_s = 0.07$ is specified. Different values of C_s were evaluated and were found to have noticeable effects on the predicted results. Finally, different values of f_k^{LES} were tested. It was found, however, that they have only a small impact on the predicted results.

The RANS region and the LES region were computed concurrently in the channel flow simulations. In the hump flow simulations, however, the entire flow was first simulated with 2D RANS. The 2D RANS results at $x = 0.6$ (60% of the hump length) were then used to prescribe the time-averaged (mean) inflow conditions for the LES simulation. As in the channel flow simulations, anisotropic synthetic fluctuations were added at the LES inlet, and the k_u and ε_u were prescribed in the same way. The embedded PANS method was found to give good results for this flow as well, but the flow recovery downstream of the recirculation region was slightly slower than in the measured flow. The effect of increased and decreased magnitude of the anisotropic synthetic inlet fluctuations was investigated. It was found that the prediction of the separation bubble on the lee side of the hump is sensitive to the magnitude of inflow fluctuations imposed. With too small, or with no, inflow fluctuations, the predicted reattachment after the recirculation bubble may become delayed due to the resolved turbulent shear stresses are small in the overall free shear layer above the recirculation region. Relatively large inflow fluctuations, on the other hand, have a significant effect on the prediction of resolved turbulent shear stresses in a short distance after the inlet in the shear layer. Moving downstream toward the reattachment location, the resolved shear layer is further re-established and bearing little historical effects of upstream inlet fluctuations, for which the turbulent shear stresses are resolved with relatively small values in part of the downstream shear layer and inducing a slightly downstream-extended reattachment location. With no inflow fluctuations, it was found that the recirculation region was poorly predicted with an over-accelerating backflow (from the reattachment location to the negative C_f peak), which is however weakened over the decelerating part in the presence of two unphysic separation bubbles.

Investigation on the effect of both the grid resolution and domain extent in the spanwise direction was conducted by doubling the number of spanwise grid cells and the spanwise extent of the computations domain. It is confirmed that the grid resolution and domain size are adequate in the baseline configuration.

Finally, the effect of the prescribed integral length scale of the synthetic inlet fluctuation was investigated. In the baseline case, it was approximately equal to the inlet boundary layer thickness. Simulations were carried out with inlet integral length scale four times smaller and twice larger, respectively, than the baseline value. As expected, a smaller (larger) turbulent inflow integral length scale induced a larger (smaller) recirculation region as a result of smaller (larger) resolved shear stresses in the free shear layer above the recirculation region.

Acknowledgments

The financial support of SNIC (the Swedish National Infrastructure for Computing) for computer time at C3SE (Chalmers Center for Computational Science and Engineering) is gratefully acknowledged. This project was financed by the EU project ATAAC (Advanced Turbulence Simulation for Aerodynamic Application Challenges), Grant Agreement No. 233710, and the Chalmers Sustainable Transport Initiative. The ATAAC project is described at `http://cfd.mace.manchester.ac.uk/ATAAC/WebHome`

References

[1] Quéméré, P. and Sagaut, P., "Zonal multi-domain RANS-LES simulations of turbulent flows," *International Journal for Numerical Methods in Fluids*, Vol. 40, No. 7, 2002, pp. 903–925.

[2] Terracol, M., "A Zonal RANS/LES Approach for Noise Sources Prediction," *Flow, Turbulence and Combustion*, Vol. 77, No. 1–4, 2006, pp. 161–184.

[3] Mathey, F. and Cokljat, D., "Zonal Multi-domain RANS/LES Simulation of Air Flow over the Ahmed Body," *Engineering Turbulence Modelling and Measurements 6*, edited by W. Rodi and M. Mulas, Elsevier, 2005, pp. 647–656.

[4] Mary, I., "Non-DES Type Hybrid RANS-LES Modelling Approaches," *Notes on Numerical Fluid Mechanics and Multidisciplinary Design*, Vol. 111, 2010, pp. 205–212.

[5] Zhang, Q., Schröder, W., and Meink, M., "A zonal RANS-LES method to determine the flow over a high-lift configuration," *International Journal of Heat and Fluid Flow*, Vol. 39, 2010, pp. 1241–1253.

[6] Ma, J., Davidson, L., Peng, S.-H., and Wang, F., "Partially Averaged Navier-Stokes Model Modelling of Turbulent Channel Flow with and without Forcing," *6th International Symposium on Turbulence, Heat and Mass Transfer*, edited by K. Hanjalic, Y. Nagano, and S. Jakirlic, 2009.

[7] Girimaji, S., "Partially-Averaged Navier-Stokes Model for Turbulence: Implementation and Validation," *43rd AIAA Aerospace Sciences Meeting and Exhibt*, 10-13 January, Reno, Nevada, 2005.

[8] Girimaji, S., "Partially-Averaged Navier-Stokes Model for Turbulence: A Reynolds-Averaged Navier-Stokes to Direct Numerical Simulation Bridging Method," *ASME Journal of Applied Mechanics*, Vol. 73, No. 2, 2006, pp. 413–421.

[9] Girimaji, S., Jeong, E., and Srinivasan, R., "Partially-Averaged Navier-Stokes Method for Turbulence: Fixed Point Analysis and Comparison With Unsteady Partially Averaged Navier-Stokes," *ASME Journal of Applied Mechanics*, Vol. 73, No. 2, 2006, pp. 422–429.

[10] Ma, J., Peng, S.-H., Davidson, L., and Wang, F., "A Low Reynolds Number Variant of Partially-Averaged Navier-Stokes Model for Turbulence," *International Journal of Heat and Fluid Flow*, Vol. 32, 2011, pp. 652–669, 10.1016/j.ijheatfluidflow.2011.02.001.

[11] Abe, K., Kondoh, T., and Nagano, Y., "A New Turbulence Model for Predicting Fluid Flow and Heat Transfer in Separating and Reattaching Flows - 1. Flow Field Calculations," *Int. J. Heat Mass Transfer*, Vol. 37, 1994, pp. 139–151.

[12] Davidson, L., "Hybrid LES-RANS: back scatter from a scale-similarity model used as forcing," *Phil. Trans. of the Royal Society A*, Vol. 367, No. 1899, 2009, pp. 2905–2915.

[13] Billson, M., Eriksson, L.-E., and Davidson, L., "Modeling of Synthetic Anisotropic Turbulence and its Sound Emission," The 10th AIAA/CEAS Aeroacoustics Conference, AIAA 2004-2857, Manchester, United Kindom, 2004.

[14] Billson, M., *Computational Techniques for Turbulence Generated Noise*, Ph.D. thesis, Dept. of Thermo and Fluid Dynamics, Chalmers University of Technology, Göteborg, Sweden, 2004.

[15] Davidson, L. and Billson, M., "Hybrid LES/RANS Using Synthesized Turbulence for Forcing at the Interface," *International Journal of Heat and Fluid Flow*, Vol. 27, No. 6, 2006, pp. 1028–1042.

[16] Davidson, L., "HYBRID LES-RANS: Inlet Boundary Conditions for Flows With Recirculation," *Advances in Hybrid RANS-LES Modelling*, Vol. 97 of *Notes on Numerical Fluid Mechanics and Multidisciplinary Design*, Springer Verlag, 2008, pp. 55–66.

[17] Davidson, L. and Peng, S.-H., "Hybrid LES-RANS: A one-equation SGS Model combined with a $k-\omega$ model for predicting recirculating flows," *International Journal for Numerical Methods in Fluids*, Vol. 43, 2003, pp. 1003–1018.

[18] Emvin, P., *The Full Multigrid Method Applied to Turbulent Flow in Ventilated Enclosures Using Structured and Unstructured Grids*, Ph.D. thesis, Dept. of Thermo and Fluid Dynamics, Chalmers University of Technology, Göteborg, 1997.

[19] van Leer, B., "Towards the Ultimate Conservative Difference Scheme. Monotonicity and Conservation Combined in a Second Order Scheme," *Journal of Computational Physics*, Vol. 14, 1974, pp. 361–370.

[20] Hoyas, S. and Jimenez, J., "Reynolds number effects on the Reynolds-stress budgets in turbulent channels," *Physics of Fluids A*, Vol. 20, No. 101511, 2008.

[21] Avdis, A., Lardeau, S., and Leschziner, M., "Large Eddy Simulation of Separated Flow over a Two-dimensional Hump with and without Control by Means of a Synthetic Slot-jet," *Flow, Turbulence and Combustion*, Vol. 83, No. 3, 2009, pp. 343–370.

[22] Saric, S., Jakirlic, S., Djugum, A., and Tropea, C., "Computational analysis of locally forced flow over a wall-mounted hump at high-Re number," *International Journal of Heat and Fluid Flow*, Vol. 27, 2006, pp. 707–720.

[23] Greenblatt, D., Paschal, K. B., Yao, C.-S., Harris, J., Schaeffler, N. W., and Washburn, A. E., "A Separation Control CFD Validation Test Case Part 1: Baseline & Steady Suction," AIAA-2004-2220, 2004.

[24] Greenblatt, D., Paschal, K. B., Yao, C.-S., and Harris, J., "A Separation Control CFD Validation Test Case Part 1: Zero Efflux Oscillatory Blowing," AIAA-2005-0485, 2005.